Revista Mexicana de Astronomía y Astrofísica, **42**, 153–166 (2006)

MODELLING OF ASYMMETRIC NEBULAE. II. LINE PROFILES

C. Morisset[1] and G. Stasińska[2]

Received 2005 November 14; accepted 2006 April 17

RESUMEN

Presentamos una herramienta, VELNEB_3D, que puede ser aplicada a resultados de códigos de fotoionización 1D o 3D para generar perfiles de líneas de emisión, mapas posición-velocidad y mapas 3D en cualquier línea de emisión suponiendo un campo de velocidad arbitrario. Presentamos algunos ejemplos, basados en nuestro pseudo-3D código de fotoionización NEBU_3D (Morisset et al. 2005) que demuestran las capacidades y la utilidad de nuestra herramienta. Un ejemplo muestra que perfiles complejos pueden ser generados con una ley de expansión simple si la nebulosa es bipolar y la rendija está ligeramente fuera del centro. Otro ejemplo muestra varias maneras de producir perfiles de líneas que pueden ser atribuidos a un campo de velocidad turbulento pero sin turbulencia en el modelo. Un tercer ejemplo muestra como en algunas circunstancias es posible discriminar entre dos estructuras geométricas muy diferentes —aquí una "ampolla de frente" y su "impostor esférico"— cuando uno usa espectros apropiados de alta resolución. Finalmente mostramos que nuestra herramienta puede generar mapas en 3D, parecidos a los que se obtienen para nebulosas extendidas observadas con unidades de campo integrado.

ABSTRACT

We present a tool, VELNEB_3D, which can be applied to the results of 1D or 3D photoionization codes to generate emission line profiles, position-velocity maps, and 3D maps in any emission line by assuming an arbitrary velocity field. We give a few examples, based on our pseudo-3D photoionization code NEBU_3D (Morisset et al. 2005) which show the potentiality and usefulness of our tool. One example shows how complex line profiles can be obtained even with a simple expansion law if the nebula is bipolar and the slit slightly off-center. Another example shows different ways to produce line profiles that could be attributed to a turbulent velocity field while there is no turbulence in the model. A third example shows how, in certain circumstances, it is possible to discriminate between two very different geometrical structures —here a face-on blister and its "spherical impostor"— when using appropriate high resolution spectra. Finally, we show how our tool is able to generate 3D maps, similar to the ones that can be obtained by observing extended nebulae with integral field units.

Key Words: **ISM: H II REGIONS — LINE: PROFILES — METHODS: NUMERICAL — PLANETARY NEBULAE: GENERAL — TURBULENCE**

1. INTRODUCTION

The study of emission line profiles in nebulae (planetary nebulae and H II regions) is important for many reasons. The shapes of emission lines result from the motions along the line of sight of the parcels of gas covered by the observational aperture and in which these lines are emitted. With the help of some hypothesis, the analysis of line profiles allows one to describe the internal motions in nebulae. It also opens access to the third dimension in the study of nebulae, since an analysis of surface brightness profiles alone may be misleading (see e.g., Morisset, Stasińska, & Peña 2005). A proper description of the geometry and kinematics of nebulae is a prerequisite to understand their dynamical evo-

[1]Instituto de Astronomía, Universidad Nacional Autónoma de México, México, D. F., México.
[2]LUTH, Observatoire de Meudon, France.

lution since the epoch of their formation. Unfortunately, the interpretation of line profiles is extremely difficult. The first spectra that showed line splitting in planetary nebulae were published by Campbell & Moore (1918) and were interpreted as due to rotation. The interpretation in terms of nebular expansion, which physically makes more sense, appeared only in 1931 (Zanstra). An extensive discussion of internal motions in planetary nebulae appears with the work of Wilson (1950). Among other things, he noted that the proportion of nebulae with split lines, in which the blue component is stronger than the red component, is equal to that of nebulae in which the reverse is occurring, which implies that the nebulae are transparent in the observed spectral range. He concluded that the relative strengths of the red and blue components depend upon non-uniform distribution of the nebular material and upon the direction of the observer. He also noted that the separation between the two components is smaller for [Ne V] than for [O III] and [Ne III] and concluded that the expansion velocity of the nebular material increases with distance to the star. This, however, was shown later not to be a general property of planetary nebulae (Sabbadin & Hamzaoglu 1982). Osterbrock, Miller, & Weedman (1966) observed emission line profiles in several bright planetary nebulae, and noted that the lines were broader than the expected thermal Doppler widths, indicating significant mass motions within the nebulae. Wilson (1958) and then Weedman (1968) were, to our knowledge, the first to perform a spatio-kinematic analysis of the data under the assumption of ellipsoidal geometry. For the five nebulae he studied, Weedman found that the expansion velocity increased with distance from the star, and that the gradient extrapolated to zero velocity at a point between the nebular shell and the center. This implies that the expansion velocity has increased since the time of ejection.

Since then, spatio-kinematic studies of planetary nebulae have gone in several directions. One is a purely empirical approach which, from observations of splitting, width and intensity ratio maps of emission lines, infers the nebular structure, using a few simplifying assumptions (Sabbadin et al. 1985): this technique has been called tomography. Other studies have focused on the kinematics of microstructures (e.g., Balick et al. 1993; Meaburn et al. 1998). On the other hand, Gesicki, Acker, & Zijlstra (2003); Gesicki & Zijlstra (2003, and references therein) have determined the internal velocity fields of about 70 planetary nebulae, by comparing observed profiles with profiles computed for 1D photoionization models, while Morisset, Gruenwald, & Viegas (2000) have developed a tool to derive morphological and kinematical information on planetary nebulae, based on a 3D photoionization code.

But 3D photoionization codes are demanding in terms of computing time, while interpretations of kinematic observational data for real planetary nebulae with a 1D tool can be misleading. Here, we present a tool, VELNEB_3D, and its association to a quick pseudo-3D photoionization code NEBU_3D (Morisset et al. 2005) which allows one to easily obtain realistic emission line profiles and radial velocity maps for any geometry.

The main goal of the present paper is to emphasize a few points:

- Emission line profiles are a combination of a morphology of the emitting gas and a velocity field. The complexity of observed line profiles can be attributed to a complex velocity law (as has been done by Gesicki et al. [2006] for years, using simple, non-realistic spherical geometry) or to a complex morphology (as commonly observed).
- Velocity fields can be partially attributed to turbulence (as claimed by Gesicki & Zijlstra 2003, for a number of planetary nebulae) simply because the analysis unduly relies on spherical models. If the models account for departure from sphericity (as ours do), there is no need of turbulence to account for the observed profiles.
- Line profiles can allow to distinguish between very different morphologies (a blister and its spherical impostor).

The structure of the paper is the following. Section 2 presents the VELNEB_3D tool and compares it to previous similar tools. The three next sections present a few applications. The main goal of the present paper is to present the capacities of this tool and no attempt is made to reproduce observations of any real object. Section 3 illustrates how complex emission line profiles can be obtained using simple expansion laws. Section 4 demonstrates how aspherical geometries can, in certain circumstances, lead to a broadening of emission lines that can be mistaken for turbulence. Section 5 shows an example where two very different geometries can be distinguished using emission line profiles. Section 6 shows an example of a 3D map in several lines generated by our code. Section 7 presents a summary and some prospects.

2. VELNEB_3D

2.1. *Description*

VELNEB_3D (which has been developed in IDL) uses the results of a 3D photoionization code. In this paper, we use the pseudo-3D photoionization code, NEBU_3D. Both NEBU_3D and the visualisation tool VISNEB_3D have been extensively described by Morisset et al. (2005). In this section we briefly recall how they operate. NEBU_3D is a set of tools that allows the user to construct a 3D photoionized model nebula from a set of runs of a 1D photoionization code (in this paper, the 1D code used is NEBU, see Morisset & Péquignot 1996; Péquignot et al. 2001). The interpolation is done on a coordinate cube for all the relevant physical parameters (electron temperature, density and ionic fractions) and for the emissivities of emission lines the user could need. After the construction is done, VISNEB_3D is used to rotate the nebula to any orientation, and to compute emission line intensity maps integrated along any line of sight.

One can then attribute a velocity vector to each cell of the coordinate cube containing the nebula. For example, one can adopt a simple radial expansion velocity law, where the magnitude of the velocity is proportional to the distance to the star, like in a Hubble flow. In each cell of the cube, the code computes elementary emission line profiles, using the velocity vector defined previously and taking into account the thermal broadening obtained from the local electron temperature and the mass of the emitting ion. A turbulence velocity can be quadratically added to the thermal velocity. An integration of the individual emission line profiles along a line of sight is performed for each pixel of the surface brightness map. The procedures used here are very similar to the ones described in more detail in Morisset et al. (2000).

Aperture effects can be simulated by applying a mask corresponding to a slit size, orientation and shift relative to the center of the image. The effect of the seeing is taken into account by smoothing the aperture mask by a given angular size square kernel. Finally, the resulting profile can also be convolved with a theoretical instrumental profile.

All this constitutes the VELNEB_3D tool, which is here applied to results from a photoionization calculation with NEBU_3D, but can be applied to results from any photoionization code. As a matter of fact, VELNEB_3D in itself is very similar to the spatio-kinematic code mentioned by Harman et al. (2004). The fact that VELNEB_3D is coupled to a photoionization code ensures that the line profiles are computed in a consistent way, taking into account the distribution of ions and temperature throughout the nebula rather than arbitrarily assuming a source function for each line.

2.2. *Comparison with Similar Tools*

We now compare the relative merits and drawbacks of several recent tools that have been designed to study nebular expansion.

Frank et al. (1993) compute 2D fully hydro simulations including photoionization. Synthetic position-velocity maps are computed and compared by eye with real observations, showing that the 2-wind model accounts qualitatively for the diversity of PN shapes and velocity fields. This is probably the most elaborate approach to study the morphodynamics of planetary nebulae. Schönberner et al. (2005) and Schönberner, Jacob, & Steffen (2005) develop a 1D hydromodelling code, including photoionization. They compare surface brightness distributions and line profiles to observations of a few planetary nebulae. One of the big limitation of these works is the spherical morphology. Rijkhorst, Mellema, & Icke (2005) performe three-dimensional AMR simulations of point-symmetric nebulae and compute PV-diagrams, but only for the hydrogen recombination lines. In addition, both this code and the Schönberner et al. (2005) code are very demanding in computing time. Morisset et al. (2000) use a static 3D photoionization code. The diffuse radiation treated in the on-the-spot (OTS) approximation —similarly to the former two groups. They apply their tool to a simple case showing how velocity field and geometry go together. The main drawback of this code is the absence of a full treatment of the diffuse field, despite the huge time of execution needed to compute a model. Harman et al. (2003) use a morphological modelling code to help determine the geometry (set to axisymmetric), structure and kinematics (a linear expansion law is used) of the ellipsoidal PN Sa 2–21. The code SHAPE (Steffen & López 2006), which works in 3D, is very versatile concerning the exploration of line profiles but, as for the code of Harman et al. (2003), the distribution of the emissivities is arbitrary and does not come from a self-consistent, photoionization approach. It must use the output of a 3D photoioinization code to improve the emissivity distribution. The main drawback of the actual version of SHAPE is the use of a commercial 3-D modelling software developed to run under the Microsoft operating system. Sabbadin et al. (2006, and references therein) claim to solve the long-standing problem of "deprojecting the bi-dimensional apparent morphology of a

three-dimensional mass of gas". They use the zero-velocity-pixel-column information to constrain 1D photoionization models and the central-star-pixel-line to constrain the expansion velocity of the emitting gas. Those techniques lead to a possible reconstruction of observed nebulae in 3D. Sabbadin et al. (2004, and references therein) use tomography to reconstruct the morphologies of PNs, but are limited by the assumption of linear expansion laws. Gesicki et al. (2006, and references therein for the same group) use a 1D static photoionization code under the OTS assumption to compute emission line profiles and compare them to observations of about 100 planetary nebulae. They allow for complex velocity fields, but are severely limited by the spherical geometry. The only fully 3D photoionization codes with accurate transfer are MOCASSIN (Ercolano et al. 2003) and the code of Wood, Mathis, & Ercolano (2004). There is no computation of line profiles yet, but VELNEB_3D can be applied to them.

Ideally, of course, one would like fully hydrodynamical, 3D models including photoionization. Even when these become available, static pseudo-3D models such as ours will remain useful to explore the parameter space because of their relative simplicity. Of the codes explicitly designed for comparison with data, the cunjunction of NEBU_3D with VISNEB so far appears to be the best compromise between relevance, versatility, and rapidity.

3. COMPLEX PROFILES WITH A SIMPLE EXPANSION LAW

3.1. *A Bipolar Nebula Toy Model*

The photoionization model presented in this section consists in applying NEBU_3D to a set of 40 runs of NEBU, each one corresponding to a different polar angular distance θ and characterized by a different gas density distribution. We consider no azimuthal variation for the density distribution. Since the model is axisymmetric, we need to model only 1/8th of the nebula, obtaining the rest of it by rotation. Thus, we vary θ from 0 to $\pi/2$, from the equator to the pole.

The inner radius, $R_{\rm inner}(\theta)$, is defined in such a way that the inner cavity has a bipolar shape, delineated by two equal intersecting spheres of radius R_2. The center of each sphere is displaced on the polar axes by a distance R_1 from the ionizing central source. The equation for the inner radius is then:

$$R_{\rm inner}(\theta) = \sqrt{R_2^2 - R_1^2 \cos^2(\theta)} + R_1 \sin(\theta)\,.$$

We assume that the hydrogen density at the inner surface is related to the distance of this surface to the ionizing star by: $n_{\rm inner}(\theta) = n_{\rm equat} \times (R_{\rm equat}/R_{\rm inner}(\theta))^2$. For each polar angle θ, the variation of the hydrogen density along the radius is given by: $n(R,\theta)_{R>R_{\rm inner}(\theta)} = n_{\rm inner}(\theta) \times (R_{\rm inner}(\theta)/R)^\gamma$ (n. b. $\gamma = 0$ corresponds to a density that is constant along each direction, $\gamma = 2$ corresponds to a free expansion in each direction). The free parameters for these geometries are then: $R_1/R_2, R_{\rm equat}, n_{\rm equat}$ and γ. For the model presented in this section, we fix R_1/R_2 so that the equatorial inner size of the nebula is half the polar inner size. This assumption implies $3R_2 = 5R_1$. We also take γ=0, and fix $R_{\rm equat}$ and $n_{\rm equat}$ so that the size of the shell is of the order of the size of the inner cavity, namely $R_{\rm equat} = 4 \times 10^{16}$ cm and $n_{\rm equat} = 3 \times 10^4$ cm^{-3}.

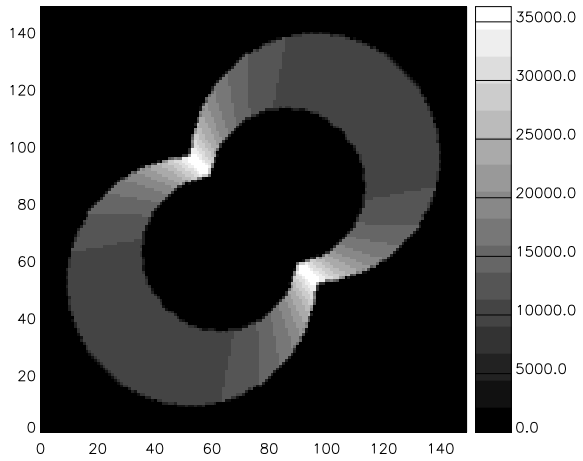

Fig. 1. Electron density distribution for the bipolar model described in § 3.1, in which the hydrogen density is kept constant along any radial direction.

The stellar energy distribution is that of a blackbody with $T_{\rm eff}$=70 kK. We adopt a stellar luminosity of L_*=1×10^{37} erg s^{-1}. The elemental abundances are taken as solar. Dust is not included in the model.

The interpolation is done in a cube of 100^3 pixels, each of 5×10^{15} cm in size. At an assumed distance of 2.7 kpc from the observer, this corresponds to an angle of 0.075″ for each pixel.

We show in Figure 1 a cut in a plane containing the polar axis, with the electron density represented by different levels of grey. Black zones correspond to null electron density (either because of lack of matter, like in the inner region, or due to the fact that no ionizing photons reach this zone, like in the outer parts). From the simple assumptions used to define the morphology of the nebula, it follows that the shape of the recombination front is bipolar, with a

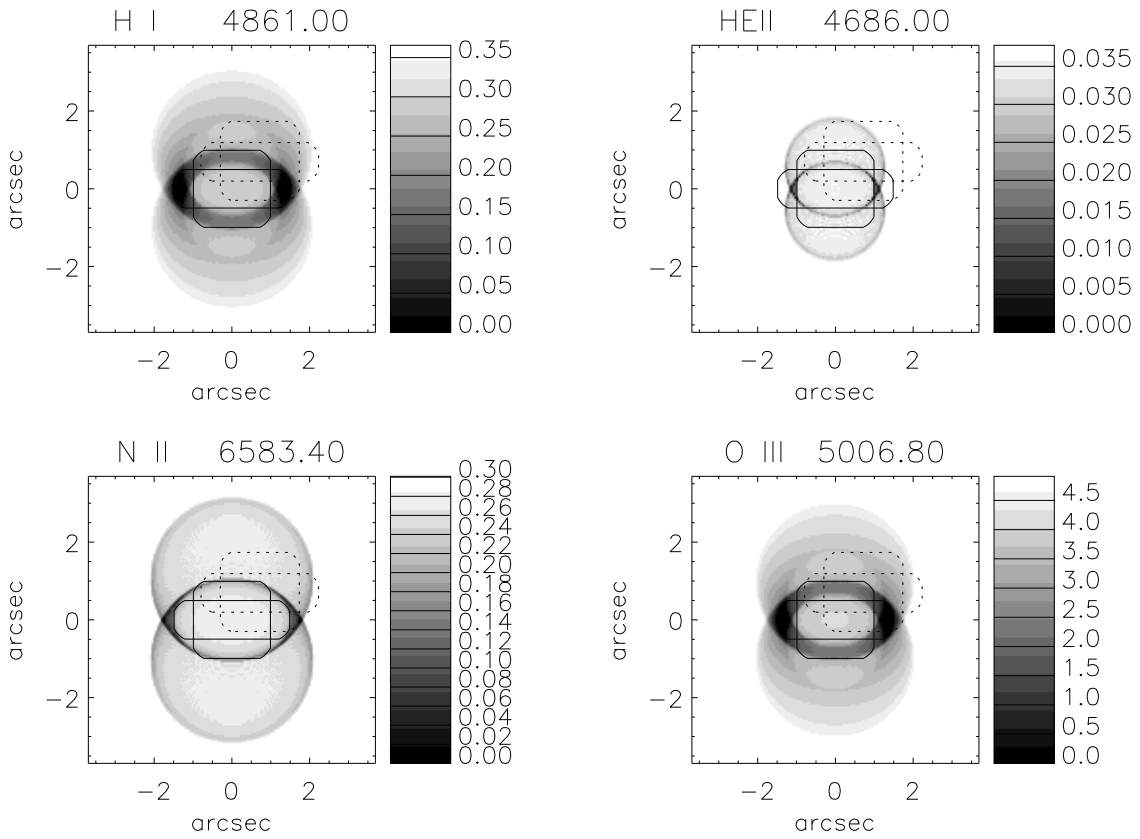

Fig. 2. Monochromatic images obtained for four emission lines (Hβ, He II 4689 Å, [N II] 6583 Å, and [O III] 5007 Å), for the bipolar nebula shown in Fig. 1 and described in § 3.1. The apertures used to compute the emission line profiles shown in Fig. 3 are superimposed on the images: the sizes of the apertures are: $1''\times 3''$ and $2''\times 2''$. The largest aperture ($10''\times 10''$) covers the entire nebula and is not shown. The centered apertures are drawn with solid lines. Off-center apertures are drawn with dashed lines. Surface brightness units are arbitrary, but the same for the four images.

strong enhancement of the density at the equatorial ring.

3.2. *Computed Monochromatic Images and Line Profiles*

The images presented in Figure 2 are computed for a nebula with a polar axis making an angle of 45 degrees with the plane of the sky. A seeing of $0.5''$ is assumed. The figure shows the surface brightness of the nebula in four emission lines: Hβ, [O III] 5007 Å, [N II] 6583 Å, and He II 4686 Å. The bipolar shape is seen in all the lines, but the images differ due to the ionization structure of the nebula. Obviously, it is the [N II] 6583 Å image which best suggests the presence of the inner cavity. There is a small "noise" (the classical "Moiré" effect) due to the finite size of the cells. This effect is also present in the surface brightness profiles shown in the next sections. This effect is more important for emission lines that are occupying a thin shell than for H I line for example. It decreases when the number of cells of the main cube increases.

The emission line profiles are computed for various apertures, indicated in Fig. 2. Solid lines correspond to centered apertures, dashed lines correspond to off-center apertures. The off-center apertures were shifted by $0.3''$ and $0.5''$ in the x- and y-directions, respectively. The proportion of the Hβ flux collected through the $1''\times 3''$ and the $2''\times 2''$ centered apertures is 18 and 19%, respectively.

To compute the line profiles, we adopted a very simple expansion velocity law, given by the following expression: $\vec{V}(\vec{R}) = V_0.\vec{R}/R_{max}$, where $\vec{R}$ is the position vector originating at the centre of the nebula, R_{max} is maximum distance of the ionization front to the center (i.e., the radius in the polar direction), and V_0 is set to 40 km s^{-1}.

The emission line profiles are computed on a 60 pixel grid (from -50 to 50 km s^{-1}).

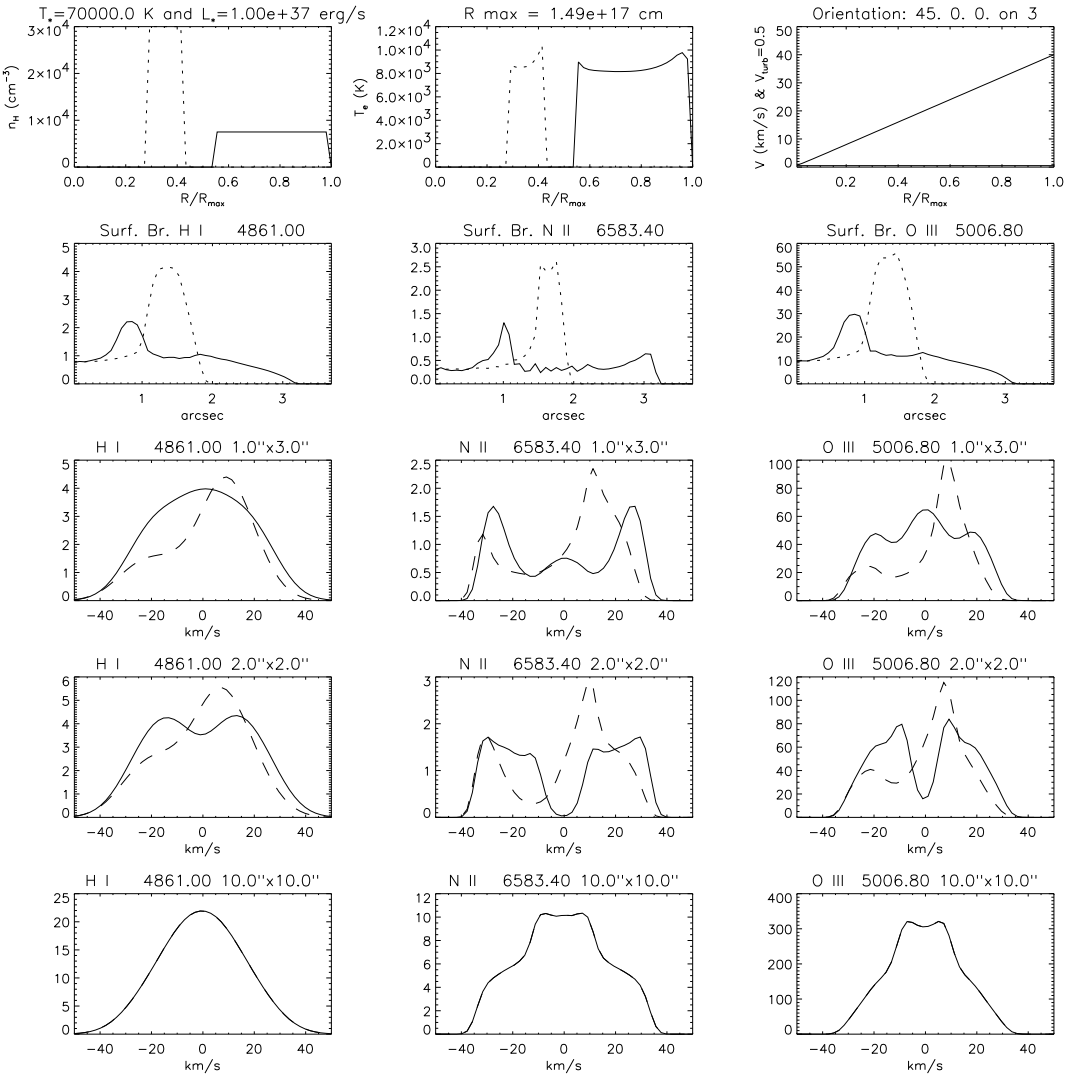

Fig. 3. Some physical parameters, surface brightness distributions and line profiles for the bipolar nebula shown in Fig. 1 and described in § 3.1. Upper row: radial distribution of the hydrogen density (left panel), the electron temperature (middle panel) and the expansion velocity (right panel). Solid curves correspond to the polar direction, dotted curves to a perpendicular one. Second row: from left to right, surface brightness distribution in the Hβ, [N II] 6583 Å and [O III] 5007 Å lines along the polar axis (solid curves) and in the perpendicular direction (dotted curves). Last three rows: from left to right, line profiles Hβ, [N II] 6583 Å and [O III] 5007 Å lines, through apertures represented in Fig. 2 (the size of the aperture is specified on top of each plot). Solid curves correspond to centered apertures, dashed curves to off-center apertures. Intensity units are arbitrary, but the same for all the plots.

The results are shown in Figure 3 for three lines: Hβ, [N II] 6583 Å, and [O III] 5007 Å (respectively left, middle and right panels of the three bottom rows). The shape and size of the slit is indicated at the top of each panel. Profiles obtained through off-center slits are represented by dashed lines. The lowest row of panels corresponds to an aperture that covers the entire nebula. This case corresponds to what would be observed for an extragalactic planetary nebula, for example. The figure also shows some plots that are useful to understand the line profiles. The top panels give the radial distribution of the hydrogen density, the electron temperature and the expansion velocity. Solid curves correspond to the polar direction, dotted curves correspond to a direction perpendicular to it. The second row of panels shows the surface brightness distribution in the Hβ, [N II] 6583 Å, and [O III] 5007 Å lines along the polar

axis (solid curves) and in the perpendicular direction (dotted curves).

As expected, the lines showing most structure are the [N II] 6583 Å ones, which are emitted in the outskirts of the nebula, and sample the largest variety of radial velocities. Note that the centered square $2''\times 2''$ aperture misses the zone of zero radial velocity (i.e., the zones where the velocity vector is entirely in the plane of the sky) while the rectangular aperture does not, leading to a very different line profile. In the case of the [O III] 5007 Å line, the rectangular slit actually intercepts a large zone with zero radial velocity, resulting in a profile without line-splitting. The Hβ line profile is the most featureless, essentially because of the strong effect of thermal velocity on this line. The important difference between the profiles of lines emitted by various ions amply justifies the use of a photoionization code to analyze the kinematics of real nebulae.

The position of the slit with respect to the center of the nebula has a dramatic influence on the observed line profiles, as can be seen by comparing the dashed and solid curves in Fig. 3. This means that a perfectly symmetric nebula can be mistaken for a nebula with uneven density distribution or complex velocity field simply because the slit is not perfectly centered!

4. MIMICKING THE EFFECT OF A TURBULENT VELOCITY FIELD

Recently, Neiner et al. (2000) and Gesicki et al. (2003) have claimed to find evidence for turbulence in certain planetary nebulae, especially in those ionized by [WC] type central stars. While it is quite possible that the strong wind from [WC] stars would induce turbulent motions in the nebular gas (see Mellema 2003), we feel that the observational evidence is not as strong as might be thought.

The effect of turbulence is to broaden the profiles by the same amount for lines of all elements. In extreme cases, this may result in the line splitting to disappear, if the broadening by turbulence is important. This is illustrated in Figures 4 and 5, which show the results from two spherical models. Both models are defined by an ionizing star of $T_{\rm eff}$=70 kK and $L_*=1\times10^{37}$ erg s^{-1} surrounded by a spherical nebula with an inner cavity of 7.5×10^{16} cm and a constant hydrogen density of 8000 cm^{-3}. The first model has a linear expansion law reaching a value of 40 km s^{-1} at the recombination front, while the second one has a turbulence of 20 km s^{-1} added, and the velocity at the recombination front is reduced to 25 km s^{-1}. In order to construct the surface brightness and velocity profile figures, a distance to the object of 1.16 kpc has been assumed, implying an outer angular radius of $8''$. The setup of the figures is the same as for Fig. 3 except that the first row has been omitted. We see in Fig. 5 that turbulence has strongly reduced the two peaks that were seen with the $3''\times 4''$ slit.

There are however several other ways to achieve such a broadening. Even in spherical symmetry, one can produce similar profiles by changing at the same time the density distribution and the expansion velocity field. Another way is to consider an ellipsoidal nebula oriented pole-on rather than a spherical one. With such a configuration, the weight of the zones of nearly zero radial velocity becomes large, and high velocity wings are produced as well. Figure 6 shows such a case, which differs from the case shown in Fig. 4 in that the nebula is now ellipsoidal with a cavity of 7.5×10^{16} cm and 1.12×10^{17} cm and an inner density of 8000 cm^{-3} and 3550 cm^{-3}, in the equatorial and polar directions respectively. The expansion law is identical and reaches a maximum velocity at the polar ionization front of 70 km s^{-1}. As seen in Fig. 6, this ellipsoidal model has line profiles very similar to the turbulent spherical model, at least if the slit size covers the whole nebula (and for Hβ, even if the slit covers a substatial part of it and is off-center). Note that even the surface brightness profiles are very similar. Therefore, nebulae that would correspond to such models would be impossible to distinguish in practice, when using observational setups such as those represented by the last two rows of Figs. 4 and 6. Note, however, that with a smaller slit, the two models can be distinguished, at least if the slit is perfectly centered (compare the second rows of Figs. 4 and 6) because in that case the splitting of the emission lines is due to crossing two emitting regions in the line of sight.

5. DISTINGUISHING A BLISTER FROM ITS SPHERICAL IMPOSTOR USING LINE PROFILES

In Paper I we showed an example where two totally different geometries could lead to the same surface brightness Hβ maps: a face-on blister could be mistaken for a sphere —which we named the "spherical impostor"[3]. Here we illustrate how high resolution spectroscopy can allow one to discriminate between the two geometries. Indeed, the velocity fields

[3]In the right panel of Figure 17 in Paper I, the line styles to represent the blister and the spherical models have been inverted: it is the blister model which was represented by a continuous line, contrary to what is stated in the legend and to what has been done for the other panels of the figure.

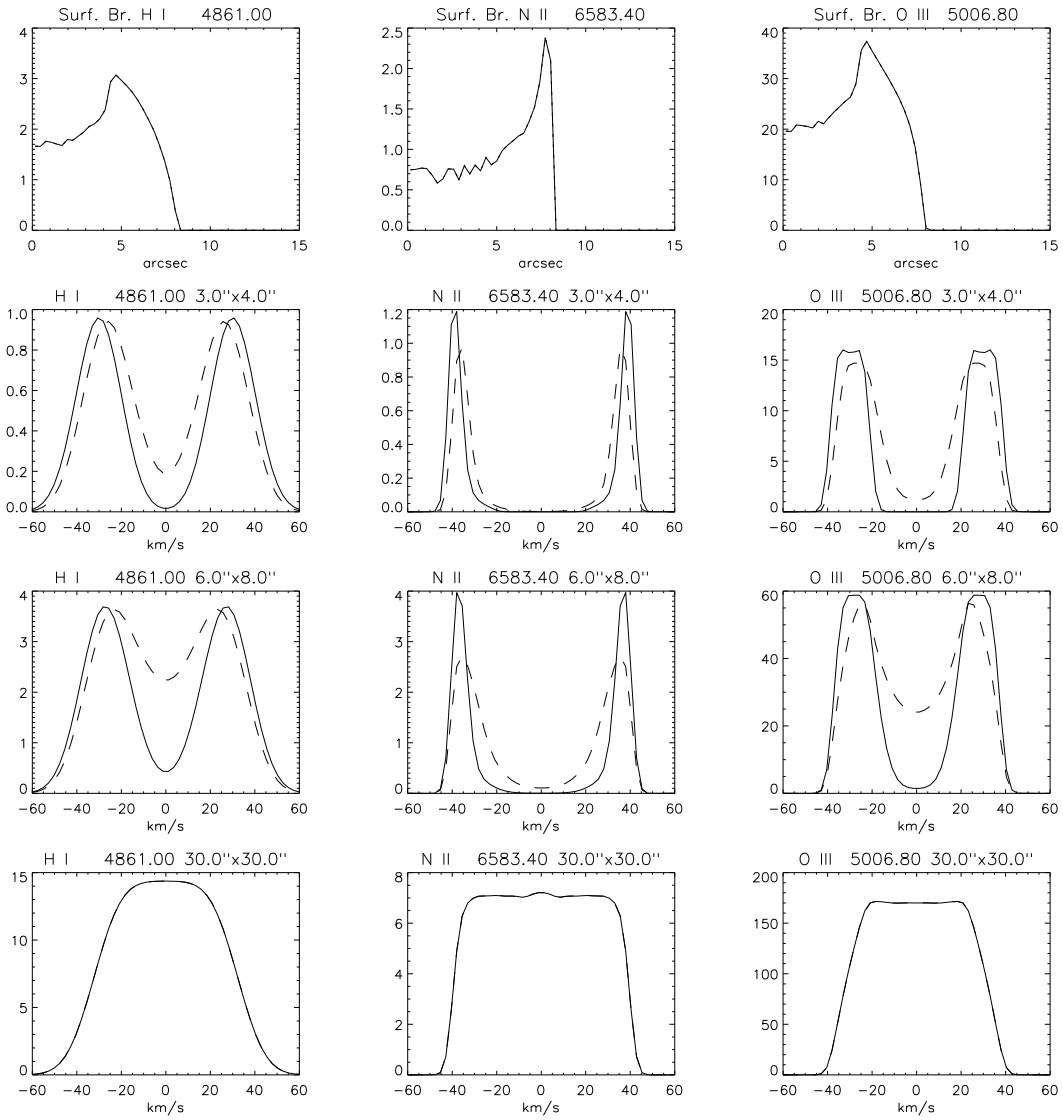

Fig. 4. Spherical nebula, with a Hubble flow expansion law and with negligible turbulence. The setup of the figure is the same as for rows 2 – 5 of Fig. 3.

for these two geometries are expected to be very different. For the face-on blister, the gas is streaming out of the neutral cloud towards the observer, while for the spherical impostor one expects a spherically symmetric expansion.

Figure 7 shows the line profiles of the blister model of Paper I, in which we have assumed that the velocity is perpendicular to the gas surface and is set to 30 km s^{-1}. Figure 8 shows the line profiles of the spherical impostor model from Paper I, in which we have assumed a constant velocity of 30 km s^{-1}. The differences between the observed profiles between Fig. 7 and Fig. 8 are spectacular. For the blister, all the lines are blue-shifted and narrow, since gas flows in only one direction. For the spherical impostor, when using a thin slit passing through the center, the emission lines are split. If the slit covers a large fraction of the object or if it is off-center, there is no splitting, but the lines are broad (their width at the base is twice the expansion velocity).

6. GENERATING 3D MAPS AND PV-DIAGRAMMS

From the examples shown in the previous sections, it is clear that the interpretation of line profiles is by no means straightforward. One of the problems is that the observed profiles strongly de-

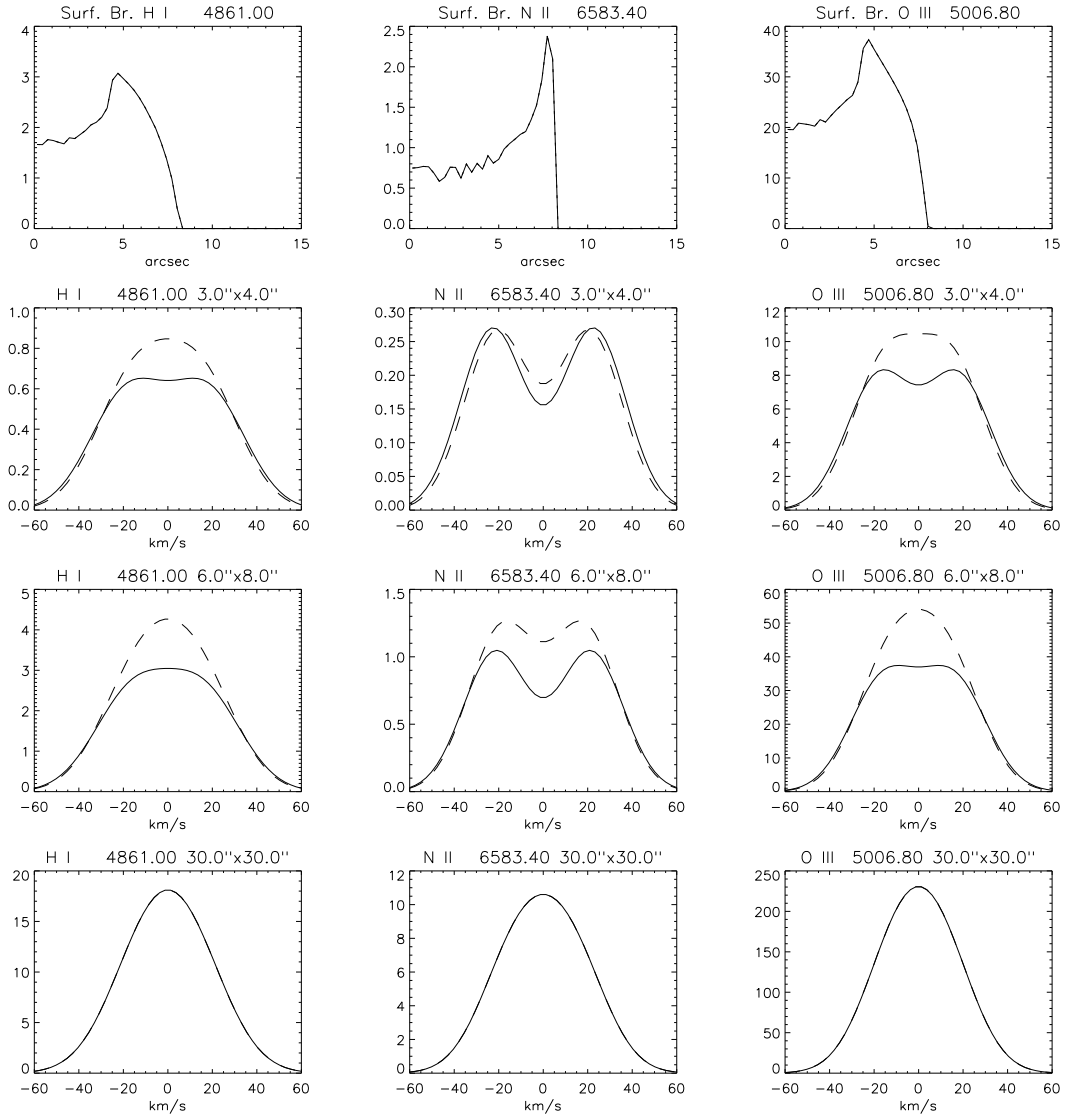

Fig. 5. Spherical nebula, with a low velocity Hubble flow expansion law and high turbulence. The setup of the figure is the same as for Fig. 4.

pend on the position and size of the slit. Obviously, a large amount of information is necessary to unambiguously unveil the morphology and kinematics of a nebula. There is now an increasing number of instruments which use integral field units (IFU) to achieve spectroscopy of an extended portion of the sky, either using lens arrays, optical fibres or image slicers. These instruments can thus generate 3D maps of extended objects, with wavelength (or velocity) being the third dimension. Such examples can be found in Ambrocio-Cruz et al. (2004) and Vasconcelos et al. (2005). Our tool is well-suited to also produce such maps for photoionization models of asymmetric nebulae. One such example is shown in Figure 9, which represents the bipolar nebula model from § 3.1. Each quadrant corresponds to a different emission line (Hβ, He II 4689 Å, [N II] 6583 Å, and [O III] 5007 Å). The grey-color image represents the surface brightness in the line, computed with pixels of $0.075'' \times 0.075''$. Superimposed on this image are the profiles of the same lines, integrated over areas of 5×5 pixels. The line intensities are all on the same scale. Apart from illustrating how the line profiles depend on the emitting ion, this figure also clearly shows how the profiles change with position. In the present case, they may change from single-peak to

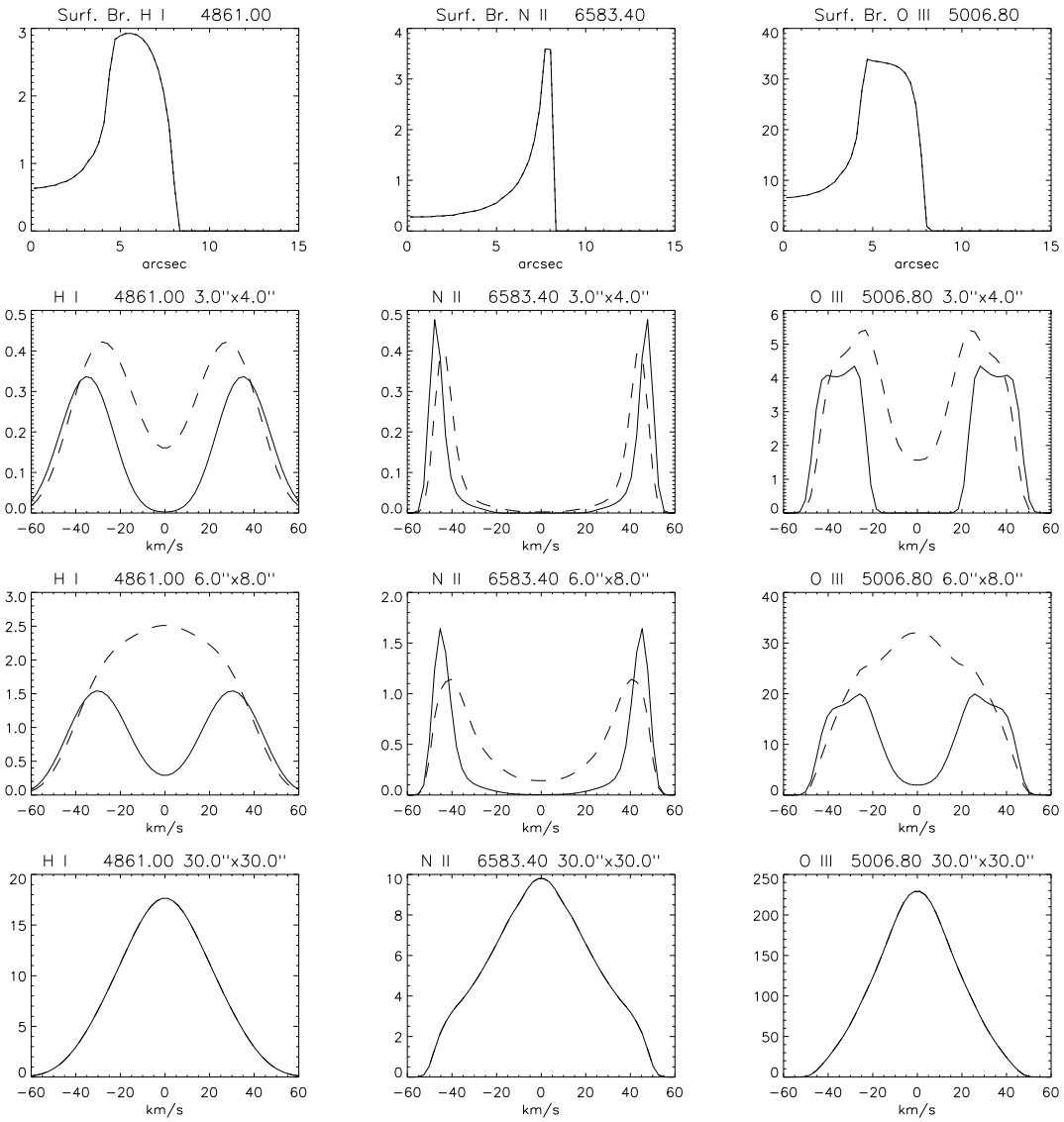

Fig. 6. Ellipsoidal nebula, seen pole-on, with a Hubble flow expansion law and without turbulence. The setup of the figure is the same as for Fig. 4.

triple-peak structures. The latter occur near the waist of the bipolar structure, when, due to inclination, the line of sight crosses the front and back of one bubble, plus the front on the other bubble (see Fig. 1 for visualization). Note that the largest component of the double-peak line profiles is the red one in the upper spectra and the blue one in the lower spectra because of the inclination of the nebula.

To illustrate the capacities of VELNEB_3D to produce Position-Velocity (PV) diagrams, the bipolar model described in § 3.1 is used to generate the images presented in Figure 10. The Hβ surface brightness map is shown with the two narrow slits superimposed, which are used to compute the PV-diagrams. One is obtained for an horizontal slit, the second one for a vertical one. They are both centered, but any position can be defined by the user. The nebula has its polar axis making an angle of 45 degrees with the plane of the sky, resulting in well defined red and blue components for the vertical slit (upper right panel of Fig. 10), when the slit is crossing the two bubbles of the nebula. This orientation effect is not seen in the case of the horizontal slit crossing mainly gas at projected velocity closed to zero (lower left panel of Fig. 10). The last panel shows a velocity channel map obtained for velocity

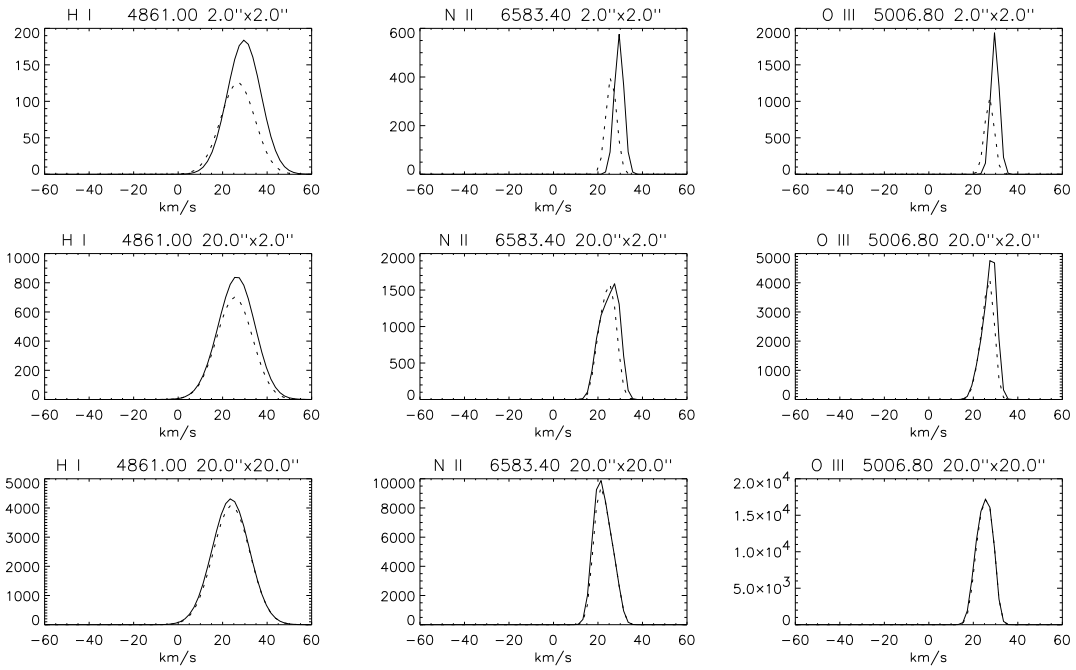

Fig. 7. Line profiles for the face-on blister (see § 5). The setup of the figure is the same asfor rows 3 – 5 of Fig. 3.

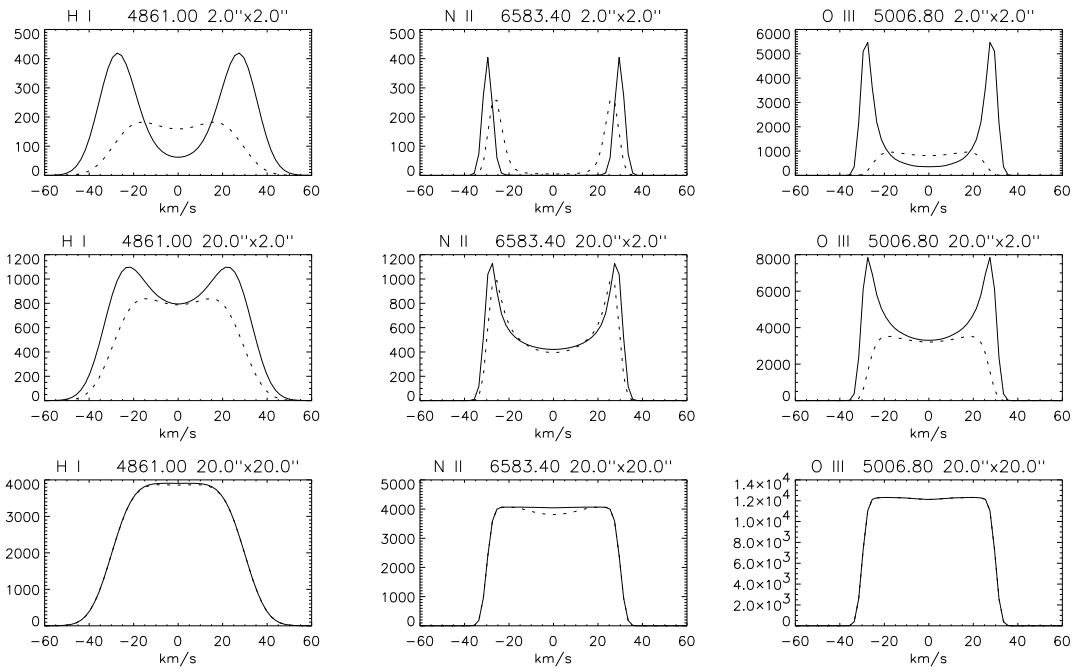

Fig. 8. Line profiles for the spherical impostor (see § 5). The setup of the figure is the same as for rows 3 – 5 of Fig. 3.

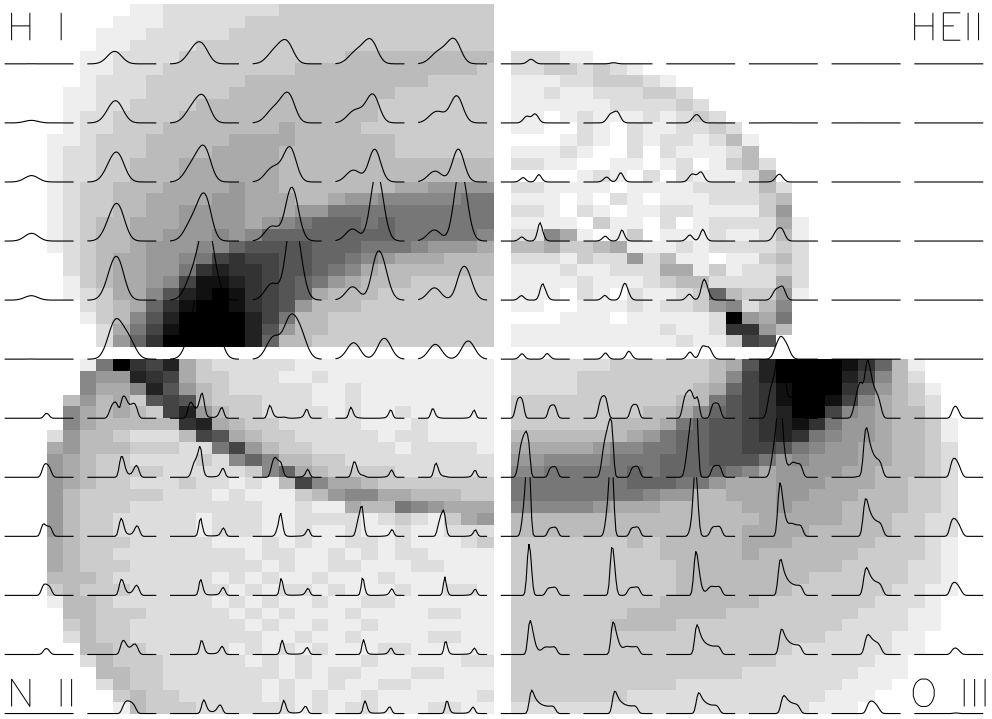

Fig. 9. A 3D map of the bipolar nebula model from § 3.1. Each quadrant corresponds to a different emission line. The surface brightness is represented by levels of grey. Superimposed on this image are the profiles of the same lines, integrated over areas of 5×5 pixels.

close to 11 km s^{-1}. The part of the nebula expanding in the positive direction is well traced.

7. SUMMARY AND PROSPECTS

In this paper we have presented a tool, VELNEB_3D, which uses the results from any 3D photoionization model to generate emission line profiles, position-velocity maps and 3D maps in any emission line by assuming an arbitrary velocity field. In this work, the code used to generate the photoionization model was NEBU_3D (Morisset et al. 2005) but any other code can be used.

So far, most of of the modelling of line profiles in planetary nebulae has been done using 1D codes (see Gesicki et al. 2003, and references therein). The examples given in this paper show that by taking into account deviations from spherical symmetry, the interpretation of the velocity field may be different. This is important, since about 80% of planetary nebulae are not round (Balick 2006).

With this tool we have been able to show how much the interpretation of observed line profiles may depend on the exact position of the slit. For example, a complex line profile may be obtained even with a simple expansion law if the nebula is not spherical and the slit is slightly off-center. Since physically, geometry and velocity field are related (the geometry being the result of the evolution of the velocity field in time) it is likely that in real nebulae with complex profiles, both the geometry and the velocity field are in fact complex. Our tool allows one to explore a larger parameter space than 1D models and (perhaps) pin down the best solution for observed nebulae. It can also be useful as a tutorial kit for those wishing to better understand observed monochromatic images and line profiles.

We believe that trying to reproduce observations of real ionized nebulae with our tool should give a better insight into the physics of these objects and guide the evolutionary dynamical modelling of planetary nebulae such as done by e.g., Villaver, Manchado, & García-Segura (2002) and Schönberner et al. (2005) in 1D and Frank et al. (1993), Mellema (1995;1997), Villaver, García-Segura, & Manchado (2003) in 2D.

While dynamical modelling is obviously the ultimate step in understanding the origin and evolution of planetary nebula shapes, or the shapes of other

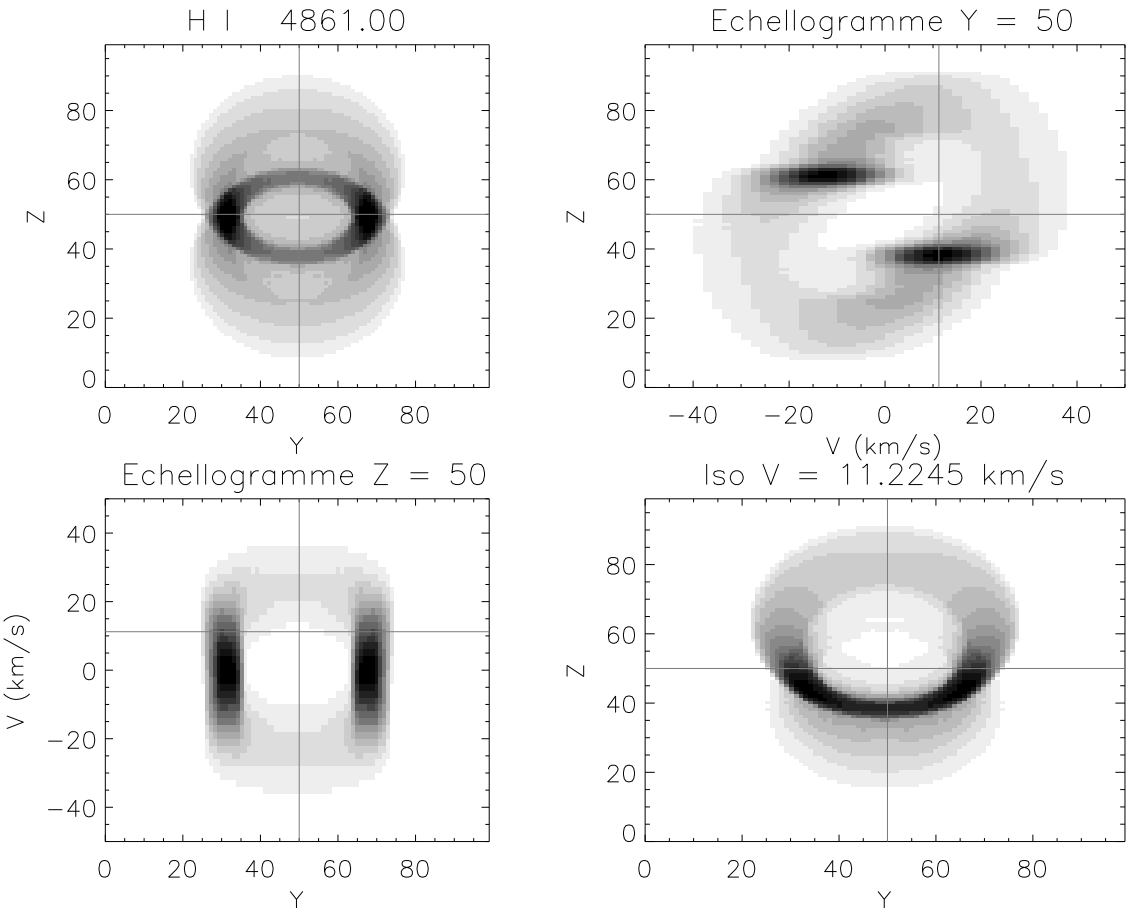

Fig. 10. PV diagrams obtained for the bipolar nebula presented in § 3.1. Upper left: surface brightness image for Hβ with the 2 slits used for the forthcoming PV diagrams, Upper right: PV diagram obtained for a narrow vertical slit crossing the center of the nebula, Lower left: PV diagram obtained for a narrow horizontal slit crossing the center of the nebula, Lower right: velocity channel map obtained from the V=11 km s^{-1} channel.

kinds of nebulae, it involves heavy computation and at the same time a simplification of the physics at work. Therefore, an exploration with a tool such as we propose is worthwhile.

Our examples suggest that it may be actually very difficult to reconstruct the geometry and velocity field of any real nebula without any underlying assumptions. However, there are cases where high resolution spectroscopy may distinguish between two very different geometries. Such is the case of a face-on blister and its spherical impostor, which have the same surface brightness distribution in Hα for the same ionizing star.

Our tool may also be useful in preparing and interpreting observations of ionized nebulae with integral field units, which are able to provide 3D maps and will predictably lead to a major progress in nebular astronomy in the coming years. We foresee, however, the difficulty that with such a huge amount of observational and computational data, it may be tough to pin down the really important physics; in other words, to not only answer the question "what is it that we see?" but also "why is it like that?" Clearly, ways will have to be found to make the best use of these tools.

Another application of our tool is the possibility to compute a large amount of models, varying the morphology, the ionization parameter, the velocity law and the position of the slit, and to include the resulting emission line profiles in a Virtual Observatory (VO). The users of the VO would be able to quickly scan the catalog to search for all the nebulae satisfying given criteria, for example on line profiles. Such a work is in progress.

The VELNEB_3D tool is available on request to C.M.

G.S. is grateful to the Instituto de Astronomía, UNAM, México, for hospitality and financial support. The computations were carried out on a AMD-64bit computer financed by grant PAPIIT IX125304 from DGAPA (UNAM, México). C.M. is partly supported by grant Conacyt-40095 (México).

REFERENCES

Ambrocio-Cruz, P., Laval, A., Rosado, M., Georgelin, Y. P., Marcelin, M., Comeron, F., Delmotte, N., & Viale, A. 2004, AJ, 127, 2145

Balick, B. 2006, in Proceedings of the Conference: Planetary Nebulae as Astronomical Tools. The Astrophysical Challenges of the Last Decade of Observations of PNE, eds. G. Stasińska & R. Szczerba

Balick, B., Rugers, M., Terzian, Y., & Chengalur, J. N. 1993, ApJ, 411, 778

Campbell, W. W., & Moore, J. H., 1918, Publications of Lick Observatory, 13, 75

Ercolano, B., Barlow, M. J., Storey, P. J., & Liu X.-W. 2003, MNRAS, 340, 1136

Frank, A., Balick, B., Icke, V., & Mellema, G. 1993, ApJ, 404, L25

Gesicki, K., Acker, A., & Zijlstra, A. A. 2003, A&A, 400, 957

Gesicki, K., & Zijlstra, A. A. 2003, MNRAS, 338, 347

Gesicki, K., Zijlstra, A. A., Acker, A., Gorny, S. K., Gozdziewski, K., & Walsh J. R. 2006, A&A, 451, 925

Harman, D. J., Bryce, M., López, J. A., Meaburn, J., & Holloway, A. J. 2004, MNRAS, 348, 1047

Harman, D. J., Bryce, M., Redman, M. P., & Holloway, A. J. 2003, MNRAS, 342, 823

Meaburn, J., Clayton, C. A., Bryce, M., Walsh, J. R., Holloway, A. J., & Steffen, W. 1998, MNRAS, 294, 201

Mellema, G. 1995, MNRAS, 277, 173

_____. 1997, A&A, 321, L29

_____. 2003, in IAU Symp. 209, Dynamics of [WR] Planetary Nebulae, eds. S. Kwok, M. Dopita, & R. Suterland (San Francisco: ASP), 507

Morisset, C., Gruenwald, R., & Viegas, S. M. 2000, ApJ, 533, 931

Morisset, C., & Péquignot, D. 1996, A&A, 312, 135

Morisset, C., Stasińska, G., & Peña, M. 2005, MNRAS, 360, 499

Neiner, C., Acker, A., Gesicki, K., & Szczerba, R. 2000, A&A, 358, 321

Osterbrock, D. E., Miller, J. S., & Weedman, D. W. 1966, ApJ, 145, 697

Péquignot, D., Ferland, G., Netzer, H., et al. 2001, in ASP Conf. Ser. Vol. 247, Spectroscopic Challenges of Photoionized Plasmas Photoionization Model Nebulae, eds. G. Ferland & D. Wolf Savin (San Francisco: ASP), 533

Rijkhorst, E.-J., Mellema, G., & Icke, V. 2005, A&A, 444, 849

Sabbadin, F., Bianchini, A., Ortolani, S., & Strafella, F. 1985, MNRAS, 217, 539

Sabbadin, F., & Hamzaoglu, E. 1982, A&A, 109, 131

Sabbadin, F., Turatto, M., Cappellaro, E., Benetti, S., Ragazzoni, R. 2004, A&A, 416, 955

Sabbadin, F. Turatto, M., Ragazzoni, R., Cappellaro, E., & Benetti, S. 2006, A&A, 451, 937

Schönberner, D., Jacob, R., & Steffen, M. 2005, A&A, 441, 573

Schönberner, D., Jacob, R., Steffen, M., Perinotto, M., Corradi, R. L. M., & Acker, A. 2005, A&A, 431, 963

Steffen, W., & López, J. A. 2006, RevMexAA, 42, 99

Vasconcelos, M. J., Cerqueira, A. H., Plana, H., Raga, A. C., & Morisset, C. 2005, AJ, 130, 1707

Villaver, E., García-Segura, G., & Manchado, A. 2003, ApJ, 585, L49

Villaver, E., Manchado, A., & García-Segura, G. 2002, ApJ, 581, 1204

Weedman, D. W. 1968, ApJ, 153, 49

Wilson, O. C. 1950, ApJ, 111, 279

_____. 1958, Reviews of Modern Physics, 30, 1025

Wood, K., Mathis, J. S., & Ercolano, B. 2004, MNRAS, 348, 1337

Zanstra, H. 1931, Zs.Ap., 2, 329

Christophe Morisset: Instituto de Astronomía, UNAM, Apdo. Postal 70-264, 04510 México, D. F., México (morisset@astroscu.unam.mx).

Grażyna Stasińska: LUTH, Observatoire de Meudon, 5 place Jules Janssen, F-92195 Meudon Cedex, France (grazyna.stasinska@obspm.fr).